Mansoura Engineering Journal

Volume 48 | Issue 3 Article 12

2023

Uses of Geographic Information Systems and Remote Sensing to Study the Natural Resource Management of the Red Sea Governorate, Egypt

Shrouk Galal
Postgraduate student in Public Works Engineering Department, Faculty of Engineering, Mansoura University, shroukhassan298015@gmail.com

Fawzi Hamid Zarzoura
Assistant professor of Public Works Engineering Department, Faculty of Engineering, Mansoura University

Mahmoud El-Mewafi
Public Works Engineering Department, Faculty of Engineering, Mansoura University, Egypt

Uses of Geographic Information Systems and Remote Sensing to Study the Natural Resource Management of the Red Sea Governorate, Egypt

Cover Page Footnote

All gratitude is due to almighty ALLAH the most gracious the most merciful who guided and aided me in bringing forth for the achievement of this thesis. I wish to express my gratitude to all who have contributed to completing this dissertation. First and foremost, I am grateful to Prof. Dr. Mahmud El-Mewafi, Professor of surveying and geodesy, Public Works Engineering Department, Faculty of Engineering, Mansoura University, for his supervision, valuable guidance, enormous help, and discussion throughout this study. I want to thank Dr. Fawzi Zarzoura, Associate Professor in the Public Works Engineering Department, Faculty of Engineering, Mansoura University, for his kind help, continuous encouragement, and advice. Last but not least, I would like to thank my family and my husband for their patience and persistent encouragement throughout my M.Sc. studies. Thanks, it must also go to the Faculty of Engineering of Mansoura University and all the teaching and non-teaching staff of the Department of Public Works Engineering.

ORIGINAL STUDY

Uses of Geographic Information Systems and Remote Sensing to Study the Natural Resource Management of the Red Sea Governorate, Egypt

Shrouk H. Galal [a,*], Fawzi H. Zarzoura [a], Mahmoud El-Mewafi [b]

[a] Public Works Engineering Department, Faculty of Engineering, Mansoura University, Egypt
[b] Surveying and Geodesy, Public Works Engineering Department, Faculty of Engineering, Mansoura University, Mansoura, Egypt

Abstract

The Red Sea governorate is rich in natural resources that create challenges for Egypt's future economy and growth. The right ways must be found to manage and discover these resources without wasting them. Remote sensing is one of the best methods used in the development of natural resources. It is based on measuring electromagnetic ray reflections from deep-seated or dispersed natural resources, and these images are processed uniquely for a variety of applications, including the detection of minerals, making land cover maps, shifting rocks, and monitoring of geological distortions. The altered rocks that existed in the study area were identified using recently developed sensors for earth observations, such as the Landsat 8 Operational Land Imager (OLI). The images have been processed using the band ratio technique and false color composite. The band ratios (red/blue, swir2/nir, swir1/nir) and spectral band combinations (Kaufmann ratio, Sabins ratio) have been used to accurately map hydrothermal alteration minerals. The OLI band ratios (6/7, 6/2, 4/5, and 6/5*4/5) have been applied to distinguish between some rocks (metavolcanic, metasedimentary, felsic, and granitic). The OLI (FCC) (6/7, 6/5, 4/2), (4/6, 4/2, 6/5), and (6/7, 4/2, 6/5*4/5) have been used to identify the minerals (Serpentine, talc-carbonate schist, quartz, and granodiorite). The methods used in this study are time, effort, and cost-saving. These methods are applicable to hard-to-reach areas. The results proved that combining spectral bands effectively identifies potential mineralization points through satellite data. Validation of these results using geological maps showed a good relationship with the location of minerals.

Keywords: Accuracy assessment, and band ratio, Landsat, Mineral exploration, Remote sensing, Supervised classification

1. Introduction

The Red Sea governorate is considered one of the most important governorates in Egypt in terms of mineral wealth. It contains the vast majority of metallic, non-metallic, and ornamental ores. These resources must be exploited and invested in to increase income, exports, and employment opportunities. Egypt's eastern desert is covered by crystalline basement rocks, from which Pharaonic miners extracted gold from Precambrian bedrock (Emra, 2006; Sabet and Bordonosov, 1984). Botros (Ns, 1991); and Wetait, 1997 observed that there were more ores and gold in Egypt. The natural resources in the study area were investigated by using the Landsat 8 Operational Land Imager (OLI) with an accuracy of 30 m (Fig. 1). Remote sensing data can be used to identify variations in surface mineralogy and structural elements (Abou El-Magd et al., 2014; Hewson et al., 2001; Okada and Ishiim, 1993). Remote sensing applications and free or low-cost satellite data that have been recently made available have enhanced scientific research and helped the industry understand the features that control mineral resources (Zoheir et al., 2019). Mineral exploration needs large amounts of manpower, a long time, and huge financial resources, especially in areas that are not accessible. A

Revised 26 January 2023; accepted 3 February 2023.
Available online 8 December 2023

* Corresponding author at: Public Works Engineering Department, Faculty of Engineering, Mansoura University, 6th District, Neighborhood 133, Building 32, 34517, Damietta, New Damietta, Egypt.
E-mail address: shroukhassan298015@gmail.com (S.H. Galal).

https://doi.org/10.58491/2735-4202.3099

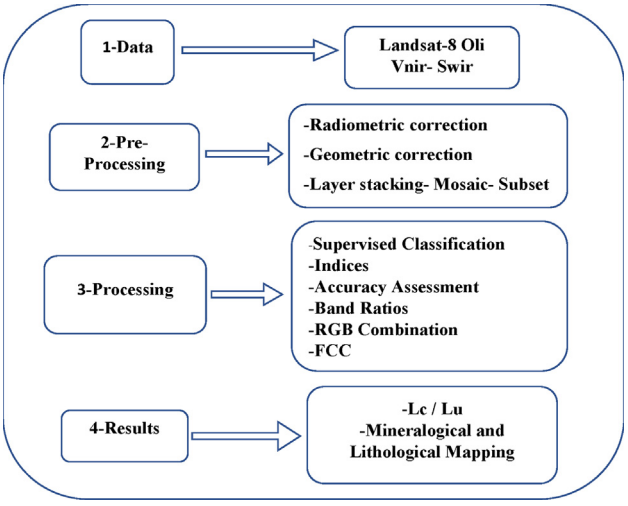

Fig. 1. Flow chart of data and methods the succession of processing steps applied for the present study.

Geographic Information System (GIS) is the greatest management tool for collecting, integrating, and organizing all these spatial data and geological maps in order to get a valuable result. Now, we can get accurate information about the mineralogy and lithology of the earth's surface and draw geological maps through remote sensing technologies and GIS easily. In this study, satellite image analysis has been used to distinguish between some rocks and minerals using the spectral properties including visible and infrared wavelengths of the rock units (Abou El-Magd et al., 2014), where rock distinction using remote sensing data depends on its chemical composition ((Abdeen et al., 2001; Velosky et al., 2003); Rowan and Mars 2003). Because of their individual spectral characteristics, which result in a precise amount of electromagnetic energy being absorbed at a particular wavelength, minerals may be located with a high degree of confidence. A common relationship with hydrothermal mineral deposits is hydrothermal variability (Mahboob et al., 2015). The Gauteng and Mpumalanga provinces of South Africa's changed rocks were mapped using open-source reflectance spectroscopy data from the multispectral moderate-resolution Landsat 8 satellite (Mahboob et al., 2019). Reducing or eliminating topographical effects by using the band ratio technique, which satellite images classify as the strongest image processing technology (Goetz et al., 1975). For image processing, the band ratio technique and false color composites (FCC) were used (Holben and Justice Co, 1981). The image and facilitates the interpretation of multispectral satellite data were improved by using the spectral band combination technique (Mahboob et al., 2019; Novak and Soulakellis, 2000). It has been demonstrated that band ratios can enhance compositional

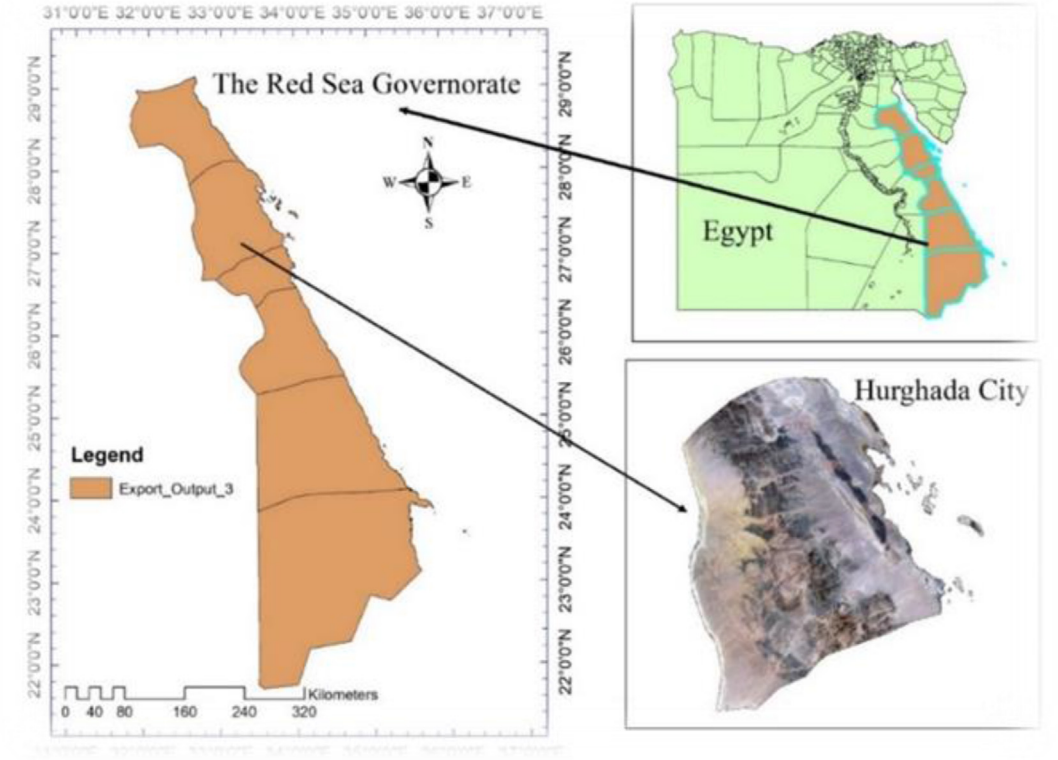

Fig. 2. Location map of the study area in Egypt.

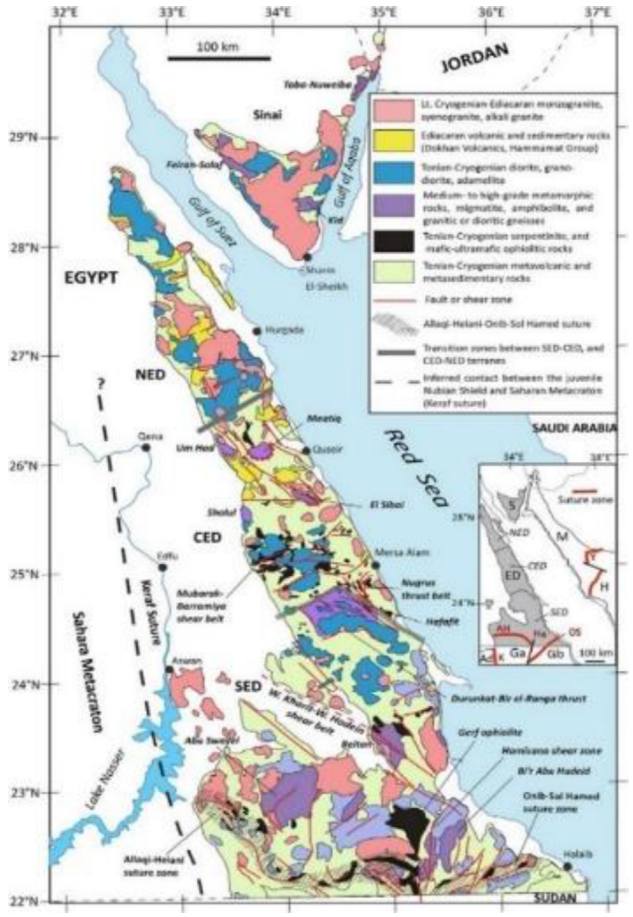

Fig. 3. Simplified geological map of eastern Desert, Egypt, (after compilation by A. –R. Fowler cited in Johnson et al., 2011).

variation while suppressing other types of information, like differences in albedo and topographic slope, that are important for lithological mapping (Mustard and Sunshine, 1998). The OLI-band ratios 6/7–6/5–4/2 were used to highlight the different rocks (Emam et al., 2018). The FCC image of three OLI-band ratios (6/7 in red (R), 6/5 in green (G), 4/2 in blue (B)) was used to distinguish the mixed serpentinite, quartz–carbonate (listvenite), and talc–carbonate schist in yellow and reddish pixels (Zoheir et al., 2019; Sabins, 1999). To highlight granitic rocks, FCC (6/7-5/6-4/2) and FCC (4/6-4/2-6/7) were used (Abrams et al., 1983). The majority of granite rocks also contain minerals like mica or amphibole.

2. Materials and methodology

2.1. Study area

Hurghada is located on the western shore of the Red Sea at longitude 33° 48′ E and latitude 27° 15′ N,

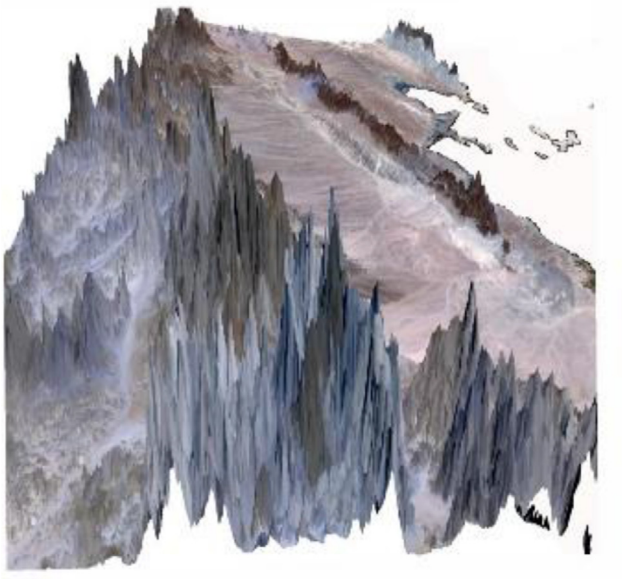

Fig. 4. Dem of study area.

as shown in Fig. 2. It is administratively affiliated with the Red Sea Governorate. It occupies 40 km of coastal strip on the western shore of the Red Sea. It covers an area of 460.5 km^2 and it is 11 m above sea level. Hurghada enjoys a moderate temperature throughout the day. Because of the dry desert climate, there are significant temperature differences between day and night, The average annual temperature ranges from 18 °C to 42 °C. The city of Hurghada and the eastern desert in general are characterized by the presence of many ores, such as granite (red rocks).

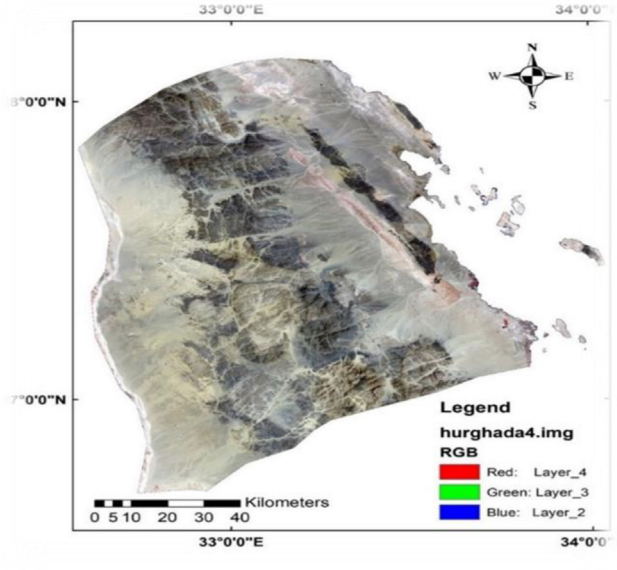

Fig. 5. Study area.

Table 1. Four landsat satellite images were used to cover study area, all images with cloud free.

RS Data (OLI)	Path/Raw	Resolution	Obtained In
LC08-L1TP	174/41	30 m	4/2020
LC08-L1TP	174/42	30 m	4/2020
LC08-L1TP	175/40	30 m	4/2020
LC08-L1TP	175/41	30 m	4/2020

2.2. Geological setting of study area

The geological map clearly shows that the study area includes phanerozoic sediments on its edges from the east and west, as shown in Fig. 3 (Zoheir et al., 2019). The study area is also one of the most remote places on Earth. It drops sharply toward the sea before gradually inching inward. The average height of the Red Sea mountains is 300–1000 m, although many of their peaks are higher than 1500 m. The highest peaks in Egypt are Jabal al-Shayeb and Jabal Hamata, with Jabal al-Shayeb 45 km southwest of Hurghada (study area). It is the highest mountain in the Red Sea and is called Everest, Hurghada has a height of 2187 m. Fig. 4 shows a digital elevation model (Dem) of the study area. This geological map shows the characteristic metavolcanics and metasedimentary rocks, alkali granite and syenogranite, in light green and pink, respectively. In Ediacaran volcanic and sedimentary rocks, cryogenian diorite and adamellite appear in yellow and blue. Granite is a plagioclase, quartz, and alkali feldspar-based, coarse-grained intrusive igneous rock. It contains magma that slowly cools and solidifies below and has a high concentration of alkali metal oxides and silica. Real granite is the granitic rock with the highest concentration of quartz, alkali felspar, and plagioclase.

Table 2. Landsat 8 satellite specteral band and spatial details.

bands	Specteral band name	Wavelenght (μm)	Spatial resolution (m)
1	Coastal aerosol	0.43–0.45	30
2	Blue	0.45–0.51	30
3	Green	0.53–0.59	30
4	Red	0.64–0.67	30
5	Near-infrared (nir)	0.85–0.88	30
6	Shortwave -infrared (Swir)1	1.57–1.65	30
7	Shortwave -infrared (swir)2	2.11–2.29	30
8	Panchromatic	0.50–0.68	15
9	Cirrus	1.36–1.38	30
10	Thermal-infrared (tirs)1	10.60–11.19	100
11	Thermal-infrared (Tirs)2	11.50–12.51	100

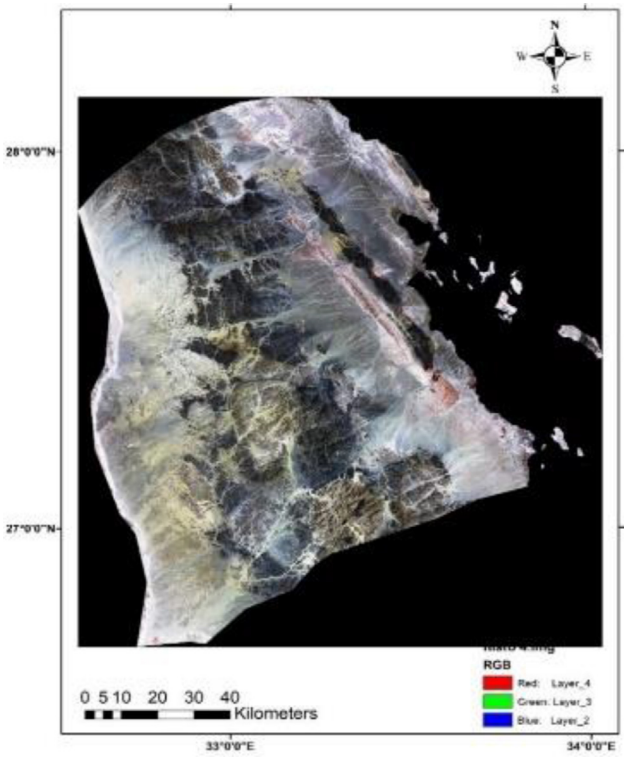

Fig. 6. Study area after corrections.

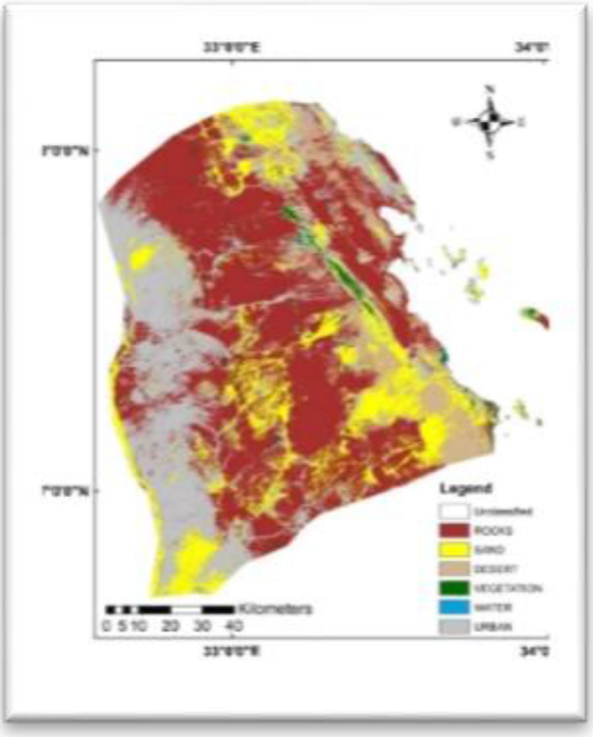

Fig. 7. Supervised classification of study area.

Table 3. Accuracy assessment for supervised classification of study area.

	Rocks	Sand	Desert	Vege-tation	Water	Urban	Total (user)
rocks	9	0	0	0	0	0	9
Sand	0	12	0	0	0	0	12
Desert	0	0	17	0	0	0	17
Vegetation	8	3	4	18	0	1	34
water	0	1	0	0	20	0	21
Urban	0	2	7	0	0	9	18
Total Producer	17	18	28	18	20	10	111

2.3. Remote-sensing data

According to (Mahboob et al., 2019), six of the Aster's sensors used for mapping and examining hydrothermal minerals stopped working in 2008. Free Landsat data is also used in the hydrothermal exploration of minerals and rocks. Wessels et al. (2013) (Fig. 5). Four Landsat satellite images were used to cover the study area (Table 1).

Cirrus is represented by OLI band 9, while coastal aerosol is represented by OLI band 1 (Mahboob et al., 2019), and thermal infrared is represented by bands 10, and 11. Therefore, these four bands were not included in further analysis. Where bands (nir, swir, and visible) are most suitable for mineral exploration (Table 2), In this study, advanced processing was done using OLI bands 2 to 7. Utilizing the layer stacking method of digital image processing, all of these bands have been combined into a single image (Mahboob et al., 2015). The data was processed using software (Erdas Imagine 2015, Arcmap 10.5, Arcscene 10.5).

3. Results and discussions

3.1. Radiometric corrections

A procedure called radiometric correction is used to reduce the values of digital numbers. The procedure calibrates or corrects distortion caused by factors such as atmospheric effects like haze or apparatus mistakes like striping in remotely sensed data. The radiometric correction must be made. This method enhances the quality and interpretability of remote sensing data, as shown in Fig. 6 (Novelli et al., 2016).

3.2. Classification

Land cover was classified into urban areas, vegetation areas, water bodies, and deserts (Muwafi

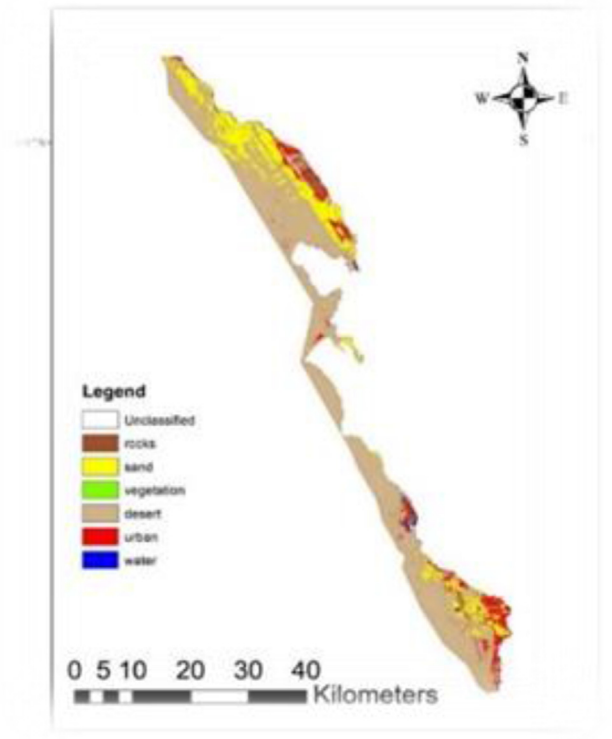

Fig. 8. Supervised classification of coastal part of study area.

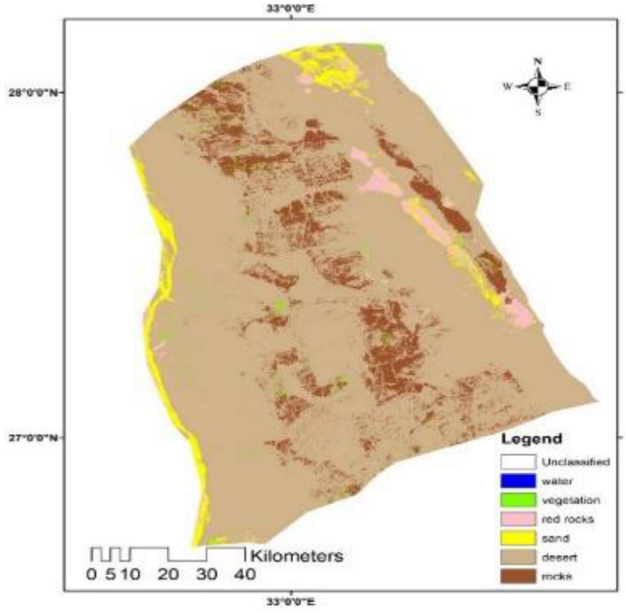

Fig. 9. Supervised classification of desert part of study area.

Table 4. Accuracy assessment.

	Rocks	Sand	Vegetation	Desert	Urban	Water	Total (user)
rocks	9	0	0	0	0	0	9
Sand	0	22	0	0	0	0	22
Vegetation	0	0	26	0	1	0	27
desert	0	0	0	46	0	0	46
urban	1	0	5	1	31	0	38
Water	0	0	0	0	0	22	22
Total Producer	10	22	31	47	32	22	164
Producer accuracy Calculation	90 %	100 %	83.87 %	97.87 %	96.87 %	100 %	
User accuracy calculation	100 %	100 %	96.29 %	100 %	81.57 %	100 %	

Table 5. Accuracy assessment.

	Water	Vegetation	Red rocks	Sand	Desert	Rocks	Total (user)
water	1	0	0	0	0	0	1
Vegetation	0	6	0	0	4	0	10
Red rocks	0	0	11	0	0	0	11
sand	0	0	0	14	0	0	14
desert	0	0	0	0	24	0	24
Rocks	0	0	0	0	0	12	12
Total producer	1	6	11	14	28	12	72

Shteiwi et al., 2021). All classification methods were carried out, and the most accurate was selected by doing an accuracy assessment (Prasomsup et al., 2020). The image was classified using the supervised classification method (Fig. 7). The classified image showed that vast areas on the Red Sea coast can be exploited, and benefited from.

3.3. Accuracy assessment

The classification accuracy was determined using the accuracy assessment model. A random set of points representing the categories on the classified map in the study area must be imposed when comparing the accuracy of land cover classification

Fig. 10. Area of shape file.

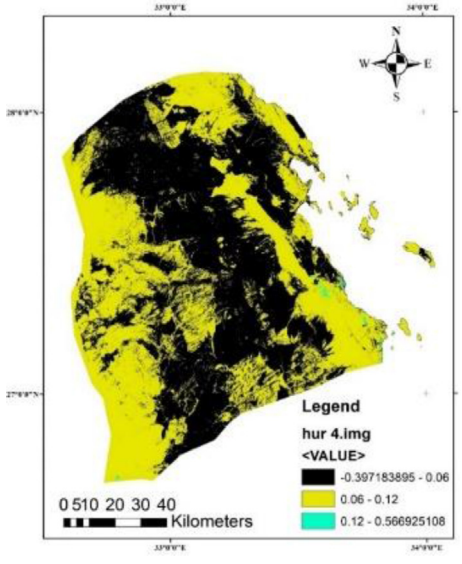

Fig. 11. Lay out of normalized difference vegetation index of study area.

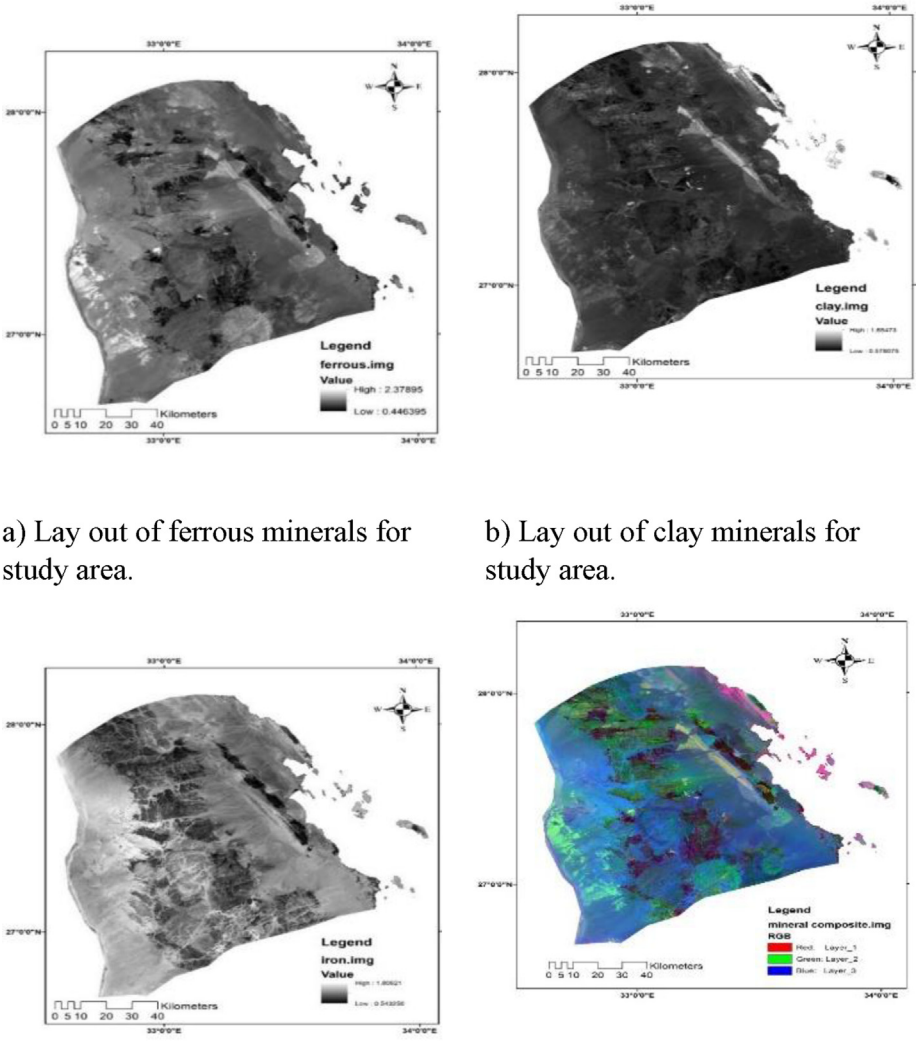

a) Lay out of ferrous minerals for study area.

b) Lay out of clay minerals for study area.

c) Lay out of iron oxide of study area.

d) Lay out of mineral composite of study area.

Fig. 12. (a, b, c, d) Lay out of indices minerals of study area.

to a higher-resolution image such as this one. from Google Earth (Borana et al., 2017) (Table 3).

Over all accuracy = total number of correctly classified pixels (Diagonal) *100/total number of reference pixels = 85/111 *100 = 76.57 %.

Kappa coefficient (T)= ((TS × TCS)-∑ (column total × row total))/(⟦TS⟧ 2- ∑ (column total-row total)) × 100.

Kappa coefficient = 74.57 %.

The results showed that the overall accuracy of land cover and kappa coefficient were unacceptable. The overall accuracy rate was poor due to a large overlap between the desert and the buildings due to the great similarity between their compositions. As a result, the study area was divided into two parts a coastal part, and a desert part, and then they were classified (Figs 8 and 9, respectively).

Accuracy assessment for coastal part of study area Table 4.

Overall accuracy = total number of correctly classified pixels (Diagonal) *100/total number of reference pixels = 156/164*100.

Overall accuracy = 95.121 %.

Kappa Coefficient (T)=((TS × TCS)-∑ (column total × row total))/(⟦TS⟧ 2- ∑ (column total*row total)) × 100.

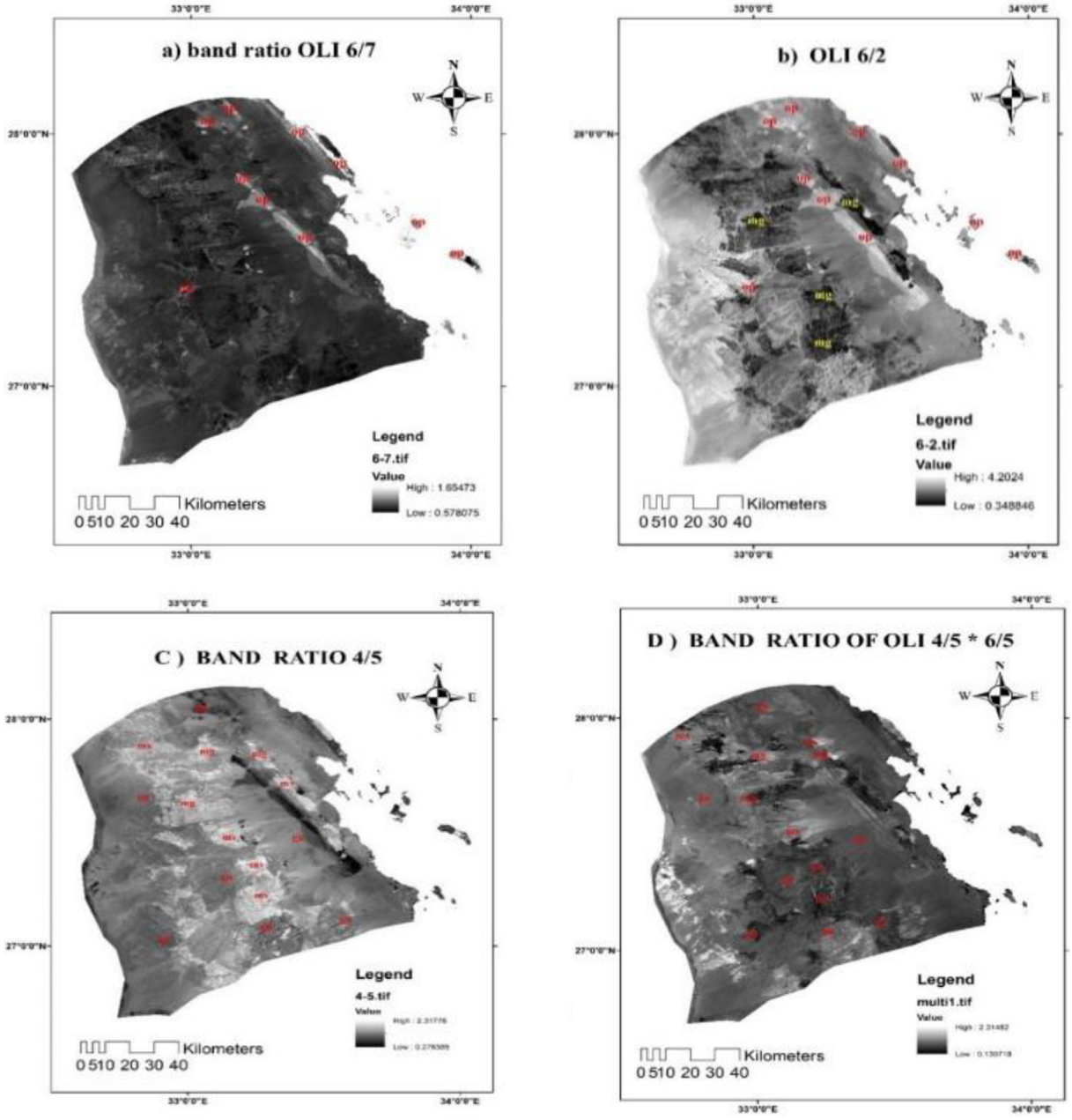

*Fig. 13. a) OLI 6/7, b) OLI 6/2 where (op) ophiolitic mélange, (Gn) granite, (Mg) metagabbro, (Mv) metavolcanics. (B) The carbonate schist, serpentinite, and graphite-bearing metasedimentary rocks are represented by the FCC (6/7 in red, 6/2 in blue, and 4/5*6/5 in green, respectively), and this image may distinguish between mafic rocks as blue pixels and felsic rocks as green pixels. (C) Pegmatites and quartz plugs can be distinguished on the OLI FCC picture (4/6, 4/2, 6/7) using colors like pale blue and cyan. pinkish and rose-colored alteration zones are those that contain anthophyllite-chlorite and talc-carbonate.*

Kappa Coefficient = 93.93 %

Area of desert = 608.27 sq.km.	Area of vegetation = 9.526 sq.km.
Area of rocks = 11.61 sq.km.	Area of sand = 140.25 sq.km.
Area of water = 10.347 sq.km.	Area of urban = 38.085 sq.km.

Accuracy assessment of desert part of study area (Table 5).

Overall accuracy = total number of correctly classified pixels Diagonal *100/total number of reference pixels = 68/72 *100 = 94.44 %.

Kappa coefficient (T)=((TS × TCS)-$\sum$ (column total × row total))/(⟦TS⟧ 2- $\sum$ (column total-row total)) × 100

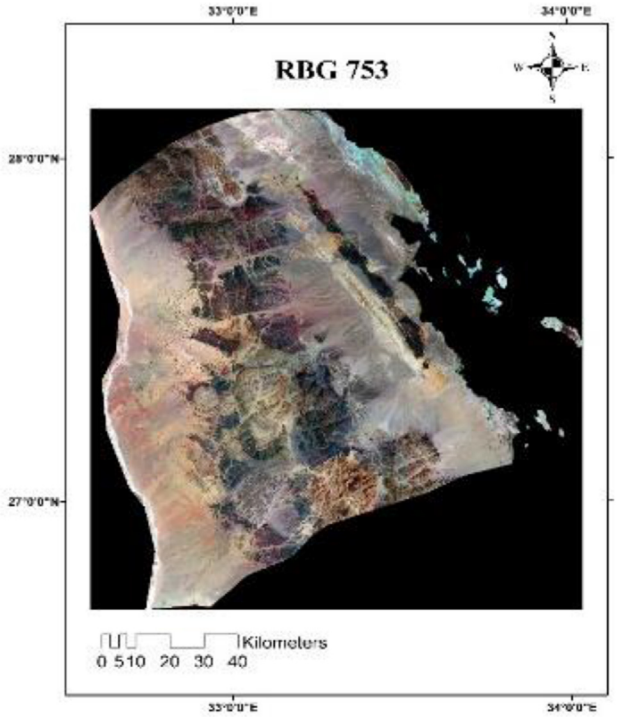

Fig. 14. RBG 753 is used to distinguish altered rocks as dazzling white, while basalt, andesite and thick-bedded volcanic conglomerate rock units are expressed dark violet.

Kappa coefficient = 92.78 %.

Area of desert = 10088.44 sq.km	Area of vegetation = 12.052 sq.km
Area of rocks = 1331.28 sq.km Area of sand = 387.42 sq.km	Area of water = 0.052 sq.km Area of red rocks = 340.898 sq.km

The area of all study area = 13090.748 sq. km as shown in shape file (Fig. 10).

Total area of rocks = 1342.89 sq.km	Total area of urban = 38.085 sq.km
Total area of desert = 10696.71 sq.km Total area of vegetation = 21.5779 sq.km Total area of water = 10.399 sq.km	Total area of sandy land = 527.677 sq.km Total area of red rocks = 340.898 sq.km Total area of classified study area = 12978.24 sq.km

All overall accuracy and kappa coefficient are acceptable.

Strength of agreement for kappa statistic 0.81–1.00 almost perfect/perfect (Borana et al., 2017).

3.4. Studied indices

Normalized Difference Vegetation Index (NDVI) has been used to identify healthy vegetation.

$$\text{NDVI equation} = (\text{NIR} - \text{RED}) \,/\, (\text{NIR} + \text{RED}).$$

NDVI values range from −1.0 to 1.0, with a positive value indicating healthy vegetation and a zero or negative value indicating anything other than vegetation. The vegetation improves with proximity to one, but it becomes worse with distance (Fig. 11).

3.4.1. Accuracy assessment

Overall accuracy = total number of correctly classified pixels (Diagonal) *100/total number of reference pixels = 60/64 *100 = 94.44 %.

3.5. Indices minerals

Ferrous minerals equation = swir1/nir (R1650/R830). Turns $fe+^{2}$- silicate-bearing into bright pixels and clearly discriminate the mafic from non-mafic (Fig. 12a).

Clay minerals equation = swir1/swir2 (R1650/R2215). The grey scale discriminates clay minerals, serpentine, and many alteration zones as bright, (b).

Iron oxide of study area equation = Red/Blue (R660/R 485). The grey scale of this ratio highlights rocks rich in hematite, (c). -Mineral composite equation = (swir1/swir2, swir1/nir, red/Blue), (d).

3.6. Band ratios

By enhancing the differences between spectral materials and reducing the effect of terrain, the band ratio method is one of the most powerful methods of digital image processing technology (Abou El-Magd et al., 2014). The data captured by Landsat 8 represents the reflective spectroscopy that can be used and exploited based on the properties of the absorption spectra for the detection of variable rocks and minerals. Each object has a unique spectral reflection of the electromagnetic spectrum. For instance, some alunite and clay ores exhibit distinctive absorption traits at about 2.1 μm and have a much better spectral response at around 1.7 μm (Mahboob et al., 2019). A set of band ratios were prepared to differentiate between the different rock units in the study area, (6/7–4/5–6/2–4/5 * 6/5) (Emam et al., 2018). Many remote sensing instruments employ frequency bands greater

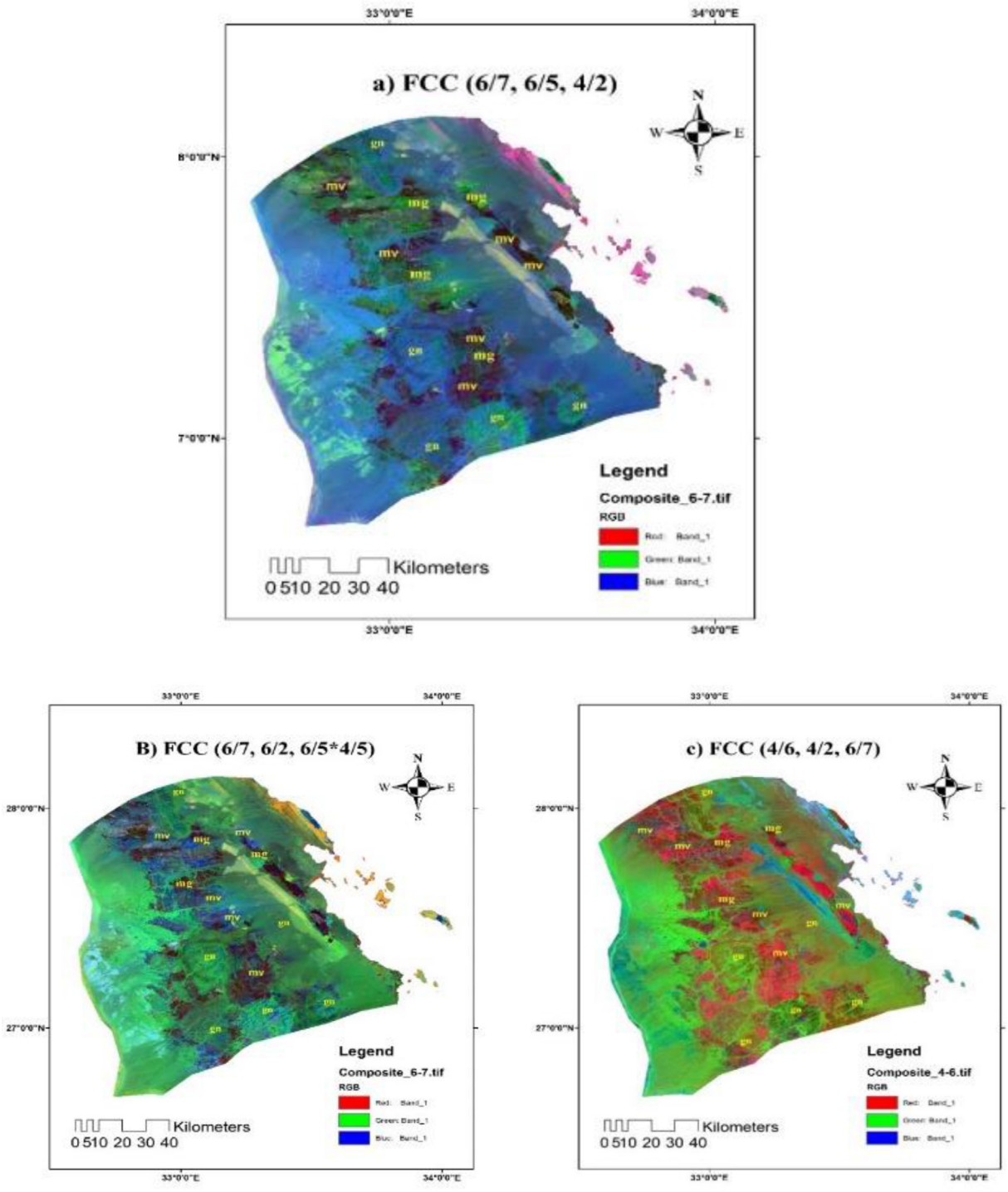

Fig. 15. (a) The mixed serpentinite, quartz carbonate (listvenite), and talk-carbonate schist are depicted in yellow and reddish pixels on the FCC image of three band ratios (6/7, 6/5, 4/2), respectively. Highly tectonized metavolcanic rocks and carbonaceous metasedimentary rocks are shown in purple and lemon colors, Granitic rocks have a bluish-green spectral signature in contrast to the dark-green spectral signature of the island arc-metavolcanic and metavolcaniclastic rocks.

than.05 m in width, which are far too broad to adequately describe the spectral absorption of various materials. Despite the fact that multispectral sensors offer additional bands, many band ratio approachs only use two or three (Mahboob et al., 2019; Meer, 2004). As a result, emphasis was placed on other advanced methods for image analysis and processing (Mahboob et al., 2019).

Fig. 13a–d shows that the OLI band ratio is 6/7, the OLI-band ratio is 6/2, the OLI band ratio is 4/5, and the OLI-band ratio is 6/5*4/5, respectively (Emam et al., 2018).

3.7. Spectral band combination

The RBG (red–green–blue) combination, also called the spectral band combination technique, helps us to improve the image and facilitates the interpretation of multispectral satellite data (Mahboob et al., 2019; Novak and Soulakellis, 2000). There are two types of band combinations: true RBG (natural) and FCC (false color composite). In this study, RBG 753 was used to distinguish altered rocks (Shirazy et al., 2020) (Fig. 14). The OLI FCC image of three band ratios (6/7 in red, 6/5 in blue, and 4/2 in green, respectively) was used to characterized the mixed serpentinite, quartz carbonate (listvenite), Granitic rocks, talk-carbonate schist, metavolcanic rocks and carbonaceous metasedimentary rocks (Sabins, 1999). The OLI FCC image (6/7, 6/2, 6/5*4/5) was used to distinguish between the different rocks (Zoheir et al., 2019). The FCC (6/7 in red, 6/2 in blue, and 4/5*6/5 in green, respectively) believes this image may distinguish between mafic rocks as blue pixels and felsic rocks as green pixels (Abrams et al., 1983).

The OLI FCC images (6/7, 6/5, 4/2), (6/7, 6/2, 6/5*4/5), (4/6, 4/2, 6/7), (6/7, 5/6, 4/2), and (6/7, 6/4, 4/2) (Fig. 15a–e), respectively, were used to identify minerals.

Validation of the results using geological maps showed a good relationship with the location of minerals and rocks.

Fig. 13a The grey scale of the band ratio of OLI 6/7 Bright pixels expresses the ophiolitic mélange. The meta-ultramafic rocks with dark grey and black tones can be distinguished most easily with an OLI-band ratio of 6/2 (b) (Fig. 16). (c, d) The difference between flesic and mafic rocks is easily distinguished by the OLI-band ratio (4/5, 6/5*4/5), while the granitoid rocks exhibit dark to medium grey tones, the ophiolitic mélange and basic metavolcanics exhibit light grey tones.

3.8. Conclusion

This study showed the simplified and effective mapping of hydrothermal minerals using Landsat reflection spectroscopic data. Various techniques have been applied to process digital images from the Landsat OLI 8 satellite. There are vast areas of unexplored landmasses on the Red Sea coast that could be exploited by oil and gas companies. Processing techniques such as the band ratio technique and the FCC (false color composite) technique (Sabins, 1999) have proven to be more important and efficient in the exploration of hydrothermal minerals, as well as in the differentiation of rocks (Liu

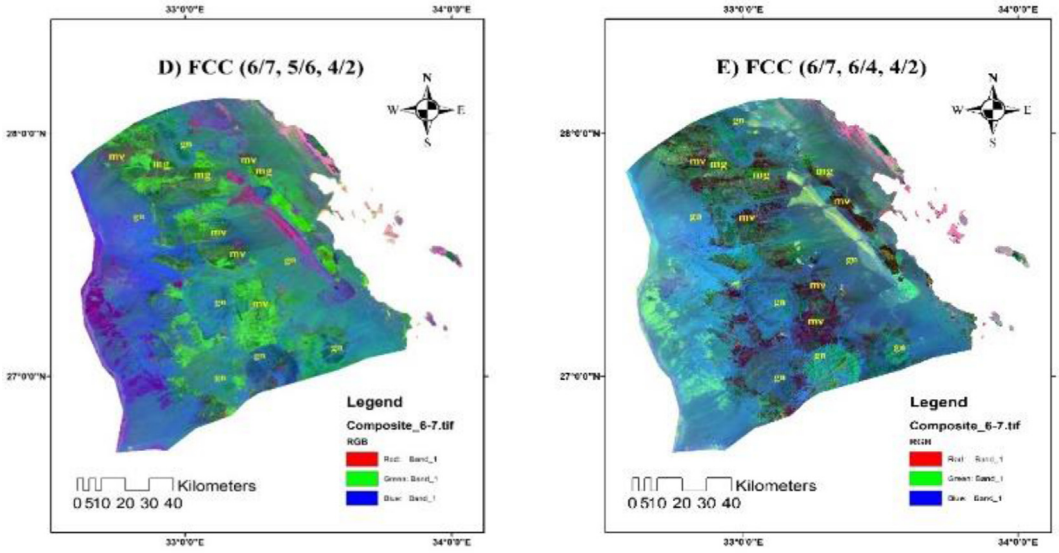

Fig. 16. (D) FCC (6/7, 5/6, 4/2), (E) FCC (6/7, 6/4, 4/2), where (Gn) granite, (Mg) metagabbro, (Mv) metavolcanic. D) Serpentine and talc-carbonate schist, which are ophiolitic mélange rocks, can be distinguished by their yellow and orange tones, while metagabbro and basic metavolcanics display a dark green hue, and hornblende-biotite gneisses and amphibolite have a brownish red hue. While pegmatitic and quartz-rich bodies have a rose hue, the chlorite-rich rocks are light green and lemon in color. Additionally, muscovite-biotite granitoids have a greenish blue color, whereas gneissic granodiorite is cyan in color. E) The OLI FCC image (6/7, 6/4, 4/2) characterized illuminated altered rocks as blue in the image; yellow color lines express vegetation.

et al., 2018; Manuel et al., 2017). GIS was used to produce maps accurately and clearly. The obtained maps showed that the study area is full of various types of granite and meta-volcanic rocks. The prepared band ratios of 4/5 * 6/5 used entirely to differentiate between mafic and felsic rocks and 6/7 used to discriminate against the ophiolitic mélange rocks (Emam et al., 2018). The OLI (FCC) (6/7, 6/5, 4/2), (4/6, 4/2, 6/5), (6/7, 6/4, 4/2) and (6/7, 4/2, 6/5*4/5) have been used to identify the minerals. The study area is full of granite of all kinds which can be used because of its many important uses. First, the maps that were produced and the minerals found in this study should be viewed as a preliminary assessment of the study region since they are simply an estimation based on techniques used in the literature for remote sensing data (Mahboob et al., 2019). Second, for Landsat 8, the spatial and spectral resolution ranges from 30 to 100 m. Datasets of this level of resolution might be sufficient for regional work but not for in-depth mineral mapping. Another factor that should be taken into consideration, the use of more precise (spatial and spectral) satellites like the World View 3 satellite or drones, which may be more appropriate for thorough mineral mapping. However, the maps created in this work provide an invaluable data source for future thorough studies (Kruse, 2015).

In this study, we present an accurate, low-cost, and time-saving way to distinguish rocks, draw geological maps, and know the locations of the most important minerals, especially for unknown or hard-to-reach areas (Wessels et al., 2013).

Authors contribution

Below is a summary of the author's statement, which shows their individual contribution to the paper based on their respective roles. 1. S H G: Data collection, tools Analysis, interpretation of data, writing an article, investigation, methodology, programs, and drafting of the material. The corresponding author is responsible for verifying the correctness, and accuracy of the descriptions and agreeing on them by all authors. 2. F H Z: Visualization and design of work, interpretation of data, supervision and revision. 3. M E-M*:* Visualization and design of the work, interpretation of data, critical revision of the article, supervision, and final revision of the text for publishing.

Funding statement

For the research, authoring, and/or publication of this paper, the authors got no financial support.

Conflicts of interest

In relation to the research, authorship, or publishing of this work, the authors declare that they have no potential conflicts of interest.

References

Abdeen, M.M., Allison, T.K., Abdelsalam, M.G., Stern, R.J., 2001. Application of Aster Band-Ratio Images for Geological Mapping in Arid Regions; the Neoproterozoic Allaqi Suture, Egypt, vol. 3. Abstract With Program Geol Soc America, p. 28.

Abou El-Magd, I., Mohy, H., Basta, F., 2014. Application of remote sensing for gold exploration in the fawakhir area, central Eastern Desert of Egypt. Arabian J. Geosci. 10.

Abrams, M., Brown, D., Lepley, L., Sadowski, R., 1983. Remote sensing for porphyry copper deposits in Southern Arizona | Azgs. Econ. Geol. 78, 591–604.

Borana, L., Yadav, S., S K, 2017. Accuracy assessment of land cover classification in Jodhpur city using remote sensing and Gis. Ijarcce 6, 10.

Emam, A., Zakaria, H., El-Fakharani, A., Ezzat, A., Gomez Barreiro, Juan, Mohammed, Y., Abo-Soliman, 2018. Utilization of aster and oli data for lithological mapping of nugrus-Hafafit area, South Eastern Desert of Egypt. Arabian J. Geosci. 11, 23.

Emra, 2006. International bid round 2006, part ii, potentiality of bid round blocks. Egyptian Mineral Resources Authority, Cairo 53.

Goetz, F.H., Billingsley, F.C., Gillespie, Ar, Abrams, Mj, Squires, R.L., Shoemaker, E.M., et al., 1975. Application of ERTS images and image processing to regional problems and geological mapping in Northern Arizona. JPL Tech. Rep. 32–1597.

Hewson, R., Cudahy, T., Huntington, J., 2001. Geologic and alteration mapping at Mt fitton, South Australia, using aster satelliteborne data. Geosci. Remote Sens. Symp. 2, 724–726.

Holben, Bn., Justice Co, 1981. An examination of spectral band ratioing to reduce the topographic effect on remotely sensed data. Int. J. Rem. Sens. 2, 115–133.

Kruse, F.A., 2015. Comparative Analysis of Airborne Visible/infrared Imaging Spectrometer (AVIRIS), and Hyperspectral Thermal Emission Spectrometer (HYTES) Longwave Infrared (Lwir) Hyperspectral Data for Geologic Mapping, pp. 480–492. https://doiorg/101117/122176646, 9472(may).

Liu, L., Yuan, L., Jun, Z., Ling, H., Xinliang, X., 2018. Gold-copper deposits in Wushitala, southern Tianshan, northwest China: application of aster data for mineral exploration. Geol. J. 53 (July), 362–371.

Mahboob, M., Iqra, A.A., Javed, I., 2015. Remote sensing and gis applications for assessment of urban sprawl in Karachi, Pakistan. Sci. Technol. Dev. 34, 179–188.

Mahboob, M.A., Genc, B., Celik, T., Ali, S., Atif, I., 2019. Mapping hydrothermal minerals using remotely sensed reflectance spectroscopy data from Landsat. J. S. Afr. Inst. Min. Metall 119, 279–289.

Manuel, R., Maria Da, G., Martim, C., Carlos, R., 2017. Remote sensing for mineral exploration in Central Portugal. Minerals 7, 184.

Meer, F.V.D., 2004. Analysis of spectral absorption features in hyperspectral imagery. Int. J. Appl. Earth Obs. Geoinf. 5, 55–68.

Mustard, J.F., Sunshine, M.J., 1998. Spectral analysis for earth science: investigations using remote sensing data. In:

Rencz, Andrew (Ed.), Remote Sensing for the Earth Sciences: Manual for Remote Sensing, third ed., pp. 251–306 3.
Muwafi Shteiwi, M., Zarzoura, F., Alebadi, Z., 2021. A comparative study of the different remote sensing techniques for evaluating land use/cover in Basra City, Iraq (Dept. C). Mej. . Mansoura Engineering Journal 45, 21–32.
Novak, I.D., Soulakellis, N., 2000. Identifying geomorphic features using Landsat-5/tm data processing techniques on Lesvos, Greece. Geomorphology 34, 101–109.
Novelli, A., Grazia, C., Eufemia, T., 2016. Evaluation of relative radiometric correction techniques on Landsat 8 Oli sensor data. In: Fourth International Conference on Remote Sensing and Geoinformation of the Environment (Rscy2016) 9688 (August): 968808.
Ns, Botros, 1991. Geological and Geochemical Studies on Some Gold Occurrences in the North Eastern Desert Egypt. ph.D. Thesis Zagazig Univ. Zagazig Egypt, p. 146.
Okada, K., Ishiim, 1993. Mineral and lithological mapping using thermal infrared remotely sensed data from Aster simulator. int geosci remote sensing symposium'. Better Understanding of Earth Environment 93, 126–128.
Prasomsup, W., Piyatadsananon, P., Aunphoklang, W., Boonrang, A., 2020. Extraction technic for built-up area classification in Landsat 8 imagery. Int. J. Environ. Sustain Dev. 11, 15–20.
Sabet, A.H., Bordonosov, V.P., 1984. The gold ore formations in the Eastern Desert of Egypt. Ann. Geol. Surv. Egypt 16, 35–42.
Sabins, F.F., 1999. Remote sensing for mineral exploration. Ore Geol. Rev. 14, 157–183.
Shirazy, A., Mansour, Z., Ardeshir, H., Timofey, T., 2020. Geostatistical and remote sensing studies to identify high metallogenic potential regions in the Kivi Area of Iran. Minerals 10 (10), 869.
Velosky, Jc., Stern, Rj., Johnson, Pr., 2003. Geological control of massive sulfidemineralization in the neoproterozoicwadi bidah shear zone, southwestern Saudi arabia, inferences from orbital remote sensing and field studies. Precambrian Res. 123, 235–247.
Wessels, R.L., Vaughan, R.G., Patrick, M.R., Coombs, M.L., 2013. High-resolution satellite and airborne thermal infrared imaging of precursory unrest and 2009 eruption at redoubt volcano, Alaska. J. Volcanol. Geoth. Res. 259 (June), 248–269.
Zoheir, B.A., Johnson, P.R., Goldfarb, R.J., Klemm, D.D., 2019. Orogenic gold in the Egyptian Eastern Desert: widespread gold mineralization in the late stages of neoproterozoic orogeny. Gondwana Res. 75 (November), 184–217.